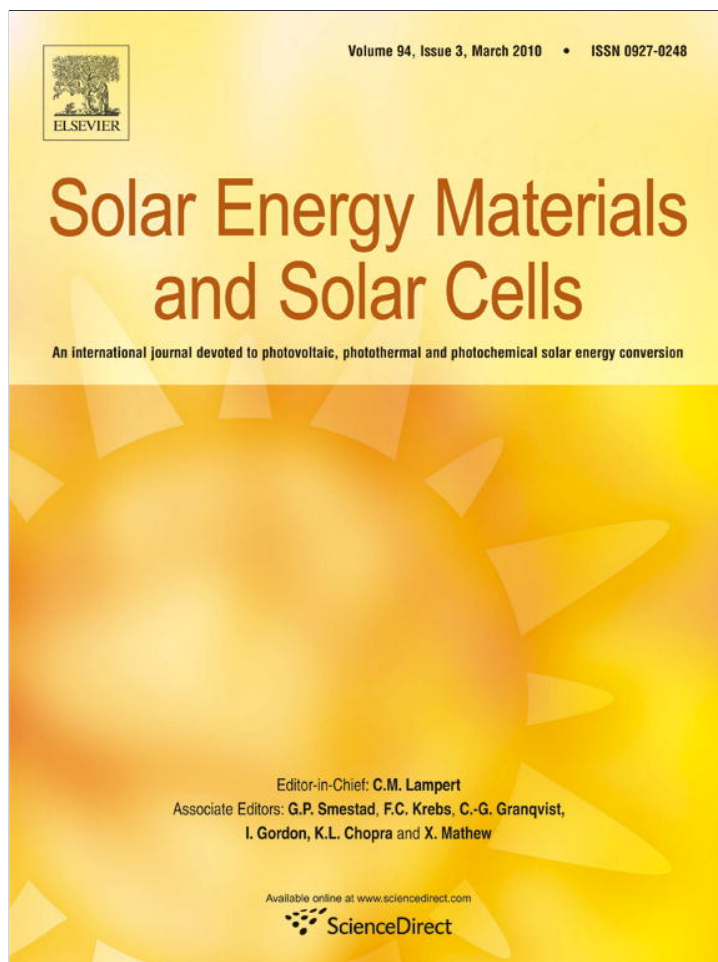


Provided for non-commercial research and education use.  
Not for reproduction, distribution or commercial use.



This article appeared in a journal published by Elsevier. The attached copy is furnished to the author for internal non-commercial research and education use, including for instruction at the authors institution and sharing with colleagues.

Other uses, including reproduction and distribution, or selling or licensing copies, or posting to personal, institutional or third party websites are prohibited.

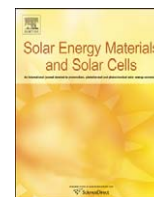
In most cases authors are permitted to post their version of the article (e.g. in Word or Tex form) to their personal website or institutional repository. Authors requiring further information regarding Elsevier's archiving and manuscript policies are encouraged to visit:

<http://www.elsevier.com/copyright>



Contents lists available at ScienceDirect

## Solar Energy Materials &amp; Solar Cells

journal homepage: [www.elsevier.com/locate/solmat](http://www.elsevier.com/locate/solmat)

## Selenization of co-sputtered CuInAl precursor films

Daniel Dwyer<sup>a,\*</sup>, Ingrid Repins<sup>b</sup>, Haralabos Efstathiadis<sup>a</sup>, Pradeep Haldar<sup>a</sup><sup>a</sup> College of Nanoscale Science and Engineering, University at Albany, State University of New York, 255 Fuller Road, Albany, NY 12203, USA<sup>b</sup> National Renewable Energy Laboratory, Golden, CO 80401, USA

## ARTICLE INFO

## Article history:

Received 2 September 2009

Received in revised form

4 December 2009

Accepted 9 December 2009

Available online 6 January 2010

## Keywords:

Selenization

CuInAl

CuInAlSe<sub>2</sub>

CIAS

CIGS

Co-sputtering

## ABSTRACT

CuInAl precursor films with varying Al/(In+Al) ratios were co-sputtered onto Mo coated soda-lime glass substrates. Metal precursor films were then selenized under vacuum conditions using thermally evaporated elemental selenium. Both precursor films and selenized samples were characterized for composition, crystalline phases, morphology, and compositional depth uniformity. Selenized films show low Al incorporation and phase separation when selenized at both 500 and 525 °C. Films selenized with a Se deposition rate of 12 Å/s showed poor adhesion compared with samples selenized at 4 Å/s. The segregation of aluminum towards the back contact as well as oxygen incorporation appears to cause adhesive loss in extreme cases, and poor interface electrical characteristics in others. The maximum device efficiency measured was 5.2% under AM1.5 for a device with ~2 at% aluminum.

© 2009 Elsevier B.V. All rights reserved.

## 1. Introduction

Much of the research on Cu-chalcopyrite absorber materials for thin film solar cells has been focused on CuInGaSe<sub>2</sub> (CIGS). In these films, gallium is substituted for indium in the CuInSe<sub>2</sub> (CIS) lattice to increase the band gap ( $E_g$ ) from ~1 eV (CIS) to as high as ~1.7 eV (CuGaSe<sub>2</sub>). Theoretically an absorber layer with an  $E_g$  ~1.4–1.45 eV would give the highest efficiency for a single junction device, however highest efficiency CIGS are limited to an  $E_g$  ~1.15 eV [1,2]. This equates to a Ga/(Ga+In) ratio of ~0.3. Increasing  $E_g$  to as high as 1.3 eV (Ga/(Ga+In)~0.5) has resulted in 15% efficient devices. As more Ga is introduced beyond this point the increase in open circuit voltage ( $V_{oc}$ ) is no longer linear with  $E_g$ , and  $V_{oc}$  is limited to ~0.8 V [3]. The photocurrent decreases as expected, and the resulting devices show decreased efficiencies.

Numerous reasons have been given for this decreased efficiency as the band gap is increased. Studies have shown that the typical CdS buffer layer may not be ideal for wide-gap materials [3,4]. As  $E_g$  is increased the conduction band offset (CBO) at the absorber/CdS interface changes from a “spike” ( $\Delta E_c > 0$ ) to a “cliff” ( $\Delta E_c < 0$ ). The ideal offset has been theorized to be  $\Delta E_c \sim +0.3$ , which is the offset for a 1.15 eV CIGS absorber. The small interface recombination velocities that occur if a  $\Delta E_c \leq 0$  results in a limit to the open circuit voltage, which is the case at a CIGS absorber band gap of 1.3–1.4 eV [3].

Defects are also thought to play a role in this decreased efficiency. Bulk defect concentration reaches a minimum at  $E_g$  = 1.1–1.2 eV, where highest efficiency devices are found. Beyond this point defect concentration rises, and reaches its maximum at 1.7 eV (CuGaSe<sub>2</sub>) [5]. Heath et al. [6] have also found a deep defect band at ~0.8 eV by transient photocapacitance spectroscopy. In low Ga samples this band lies close to the conduction band. As Ga is increased the band moves closer to the mid-gap, and should become a much more efficient recombination center. These defects could be responsible for the limited efficiencies of high-Ga CIGS devices.

Aluminum can also be used to alter the band gap of CIS. CuInAlSe<sub>2</sub> (CIAS) films have an  $E_g$  range of ~1 eV (CuInSe<sub>2</sub>) to ~2.7 eV (CuAlSe<sub>2</sub>). The ~0.8 eV deep defect band found in CIGS is not present in CIAS films. Increasing Al content does increase the Urbach energy of the band tail, suggesting an increased disorder to the material, but the lack of a deep defect band is favorable for the production of wide-gap CIAS devices [7].

Aluminum also produces a larger band gap change in CIS than Ga due to the smaller size of the Al atom. For instance a band gap of 1.4 eV requires Ga/(Ga+In) ~0.55 in CIGS, and only Al/(Al+In) ~0.22 in CIAS. This should result in reduced lattice deformation in CIAS, which may lead to fewer structural defects associated with higher gap films [8].

Record CIAS lab scale device efficiency has reached 16.9% using a co-evaporation process [9]. An alternative method to co-evaporation that has produced device quality CIS and CIGS films is sequential or co-sputtering of metal precursors, followed by selenization in a selenium atmosphere [10–13]. Of the two sputtering methods, co-sputtering allows for greater compositional depth uniformity

\* Corresponding author. Tel.: +1 518 796 6768.

E-mail address: [DDwyer@uamail.albany.edu](mailto:DDwyer@uamail.albany.edu) (D. Dwyer).

through control of metal precursor deposition conditions. The sputtering/selenization process is believed to be easier to scale up to a high throughput-manufacturing environment where monolithic modules must be uniform in thickness and composition over large deposition areas.

Potential applications for CIAS include both single and multi-junction devices. A  $\text{CuInSe}_2$  bottom absorber, combined with one or two CIAS absorbers of wider band gap would be ideal for space applications where the inherent radiation resistance of the chalcopyrite structure, along with the high specific power (W/kg) of a thin film multi-junction cell is desired. Films could also be used as an alternative to CIGS if similar efficiencies can be produced using the sputtering/selenization approach.

For this paper precursor films were co-sputtered from Cu, In, and Al targets, and then selenized using thermally evaporated elemental selenium. The results of different selenization parameters on film properties, as well as some current challenges associated with the development of sputtered/selenized CIAS films will be presented.

## 2. Experimental

### 2.1. Precursor deposition

Metal precursor films for this work were deposited on  $1 \times 3''$  molybdenum coated soda-lime glass (Mo/SLG) substrates. The Mo back contacts, as well as metal precursor films, were deposited using an AJA International Inc. ATC magnetron sputtering system equipped with three 3" sputtering guns. Sputtering guns are positioned in a con-focal arrangement allowing simultaneous deposition of precursor elements, while stage rotation maintains film thickness and compositional uniformity.

Mo films were deposited by DC magnetron sputtering to a thickness of  $\sim 1 \mu\text{m}$ . The Mo/SLG was then moved to the load lock for storage, targets were changed, and the system was pumped down to a base pressure of  $\sim 5 \times 10^{-7}$  Torr. A target sputter clean was performed first to remove any surface oxides, or contaminant layers. Single target sources of Cu, In, and Al were then used to deposit the precursor film in a layered co-sputtering approach onto the Mo/SLG substrates. The phase "layered co-sputtering" is used because the metals are sputtered both individually (layered sputtering), as well as simultaneously (co-sputtering), where two or all three metals are sputtered at the same time.

A drawing of a typical layered co-sputtering deposition is shown in Fig. 1. Deposition began by co-sputtering Cu–In. This was followed by Cu–In–Al. One thousand seconds before the end the deposition both the Al and In guns were shut down, and Cu was sputtered alone to form a capping layer ( $\sim 100 \text{ nm}$  thick) to prevent Al oxidation. The exact start time for Al and end time for In were varied to obtain different Al/(Al+In) ratios. The power density ( $\text{W}/\text{cm}^2$ ) of the Al and In guns were adjusted to fine tune film compositions. A more detailed description of the precursor deposition can be found in previous work [14].

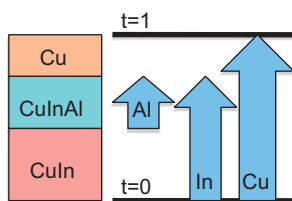


Fig. 1. Depiction of the layered co-sputtering process used in precursor deposition. The arrows indicate the metal being sputtered, with the deposition beginning at  $t=0$  and ending at  $t=1$ .

### 2.2. Selenization

Selenization of metal precursors was performed in a turbo-pumped thermal evaporation setup with a base pressure of  $\sim 1 \times 10^{-6}$  Torr. Here, a heated baffled box source was used to evaporate elemental selenium while the deposition rate was maintained through closed-loop feedback with a quartz crystal monitor. Substrates were positioned on  $2 \times 2''$  boron-nitride masks and heated with tungsten-halogen lamps from the back surface. A thermocouple positioned on the back of a sample was used to measure the film temperature and feedback to the lamps PID controller. The system is not load-locked so after the selenization process a nitrogen purge and pump cycle was used to flush any selenide gases before samples were removed.

The temperature ramp rate was maintained at  $\sim 50^\circ\text{C}/\text{min}$  for all depositions. Deposition time, temperature, and selenium flux ( $\text{\AA}/\text{s}$ ) were varied to determine the effect of different process parameters on film properties. Films were finished by depositing CdS by chemical bath deposition of CdS to a thickness of  $\sim 60 \text{ nm}$ . i-ZnO was then RF-sputtered to a thickness of  $\sim 100 \text{ nm}$  followed by  $\sim 200 \text{ nm}$  of ZnO:Al. Ni ( $\sim 50 \text{ nm}$ )/Al ( $\sim 3 \mu\text{m}$ ) metal grids were then deposited by electron beam evaporation.

### 2.3. Film characterization

Film compositions were measured using a JEOL Superprobe 8600 electron microprobe equipped with four wavelength dispersive spectrometers (WDS) and one energy dispersive spectrometer (EDS). Electron probe microanalysis (EPMA) uses standards of relevant elements to provide accurate compositional analysis of bulk materials. EPMA is necessary for CIAS films because its energy resolution ( $\sim 5 \text{ eV}$ ) is needed to separate the Al  $K\alpha$  (1486.6 eV) and Se  $L\alpha$  (1379 eV) X-ray peaks. The energy resolution of a typical EDS is around 130 eV depending on the X-ray being analyzed [15]. Precursor films were measured at an accelerating voltage of 15 kV, and selenized films at 20 kV.

While EPMA provides accurate bulk compositions, it is limited to the interaction volume of the electron beam and the energy of the X-ray line of each element. If the film is not uniform in composition with depth the resulting composition favors those elements at the surface and/or with higher energy X-ray lines that are capable of escaping from greater depths. To measure the change in composition with depth Auger electron spectroscopy (AES) was performed using a Physical Electronics model 15–110B cylindrical mirror analyzer. Primary electron energy of 5 keV was used at a current of  $\sim 1 \text{ mA}$ . Sputtering time was 2 min between each surface analysis.

To determine the chemical state of the film elements X-ray photoelectron spectroscopy (XPS) was used. A ThermoVG Thetaprobe equipped with a hemispherical analyzer and a monochromated Al  $K\alpha$  X-ray source was operated at a 100 W/200  $\mu\text{m}$  spot mode. Pass energy for surveys was 300 eV. Due to the film thickness a wide sputter crater was formed using the ion gun on the AES system, and then the sample was transferred to the XPS system. The crater wall was used to access the different depths in the film. The surface of the analysis area was sputtered to remove surface oxides and data were taken. The XPS chamber was maintained at  $2 \times 10^{-9}$  Torr during analysis, except during argon introduction.

Crystalline phases were determined with X-ray diffraction (XRD). XRD scans were carried out on a Scintag X-ray diffractometer equipped with a Cu  $K\alpha$  X-ray source and a horizontal wide-angle four-axis goniometer with stepping motors which allowed independent or coupled  $\theta/2-\theta$  axes motion. Precursor films were scanned from  $25^\circ$  to  $50^\circ$ , and selenized films from  $20^\circ$  to  $60^\circ$ . Grazing-incidence X-ray diffraction (GIXRD) measurements

with omega set at 2° were also used to determine if any phase changes occurred between the bulk and surface regions. The collected XRD measurements were compared with reference patterns from the standard Joint Committee for Powder Diffraction Standards (JCPDS) powder diffraction file (PDF).

To determine the amount of Al incorporated into the CIS structure a targeted scan of the (1 1 2) peak of each film was run. A NIST calibrated flat plate standard with a peak location at 26.649° was used to ensure tool shift did not affect peak measurements. According to Vegard's law there should be a linear shift in the lattice spacing between CIS ( $2\theta=26.624^\circ$ ) and CAS ( $2\theta=27.732^\circ$ ) with increasing Al concentration [16]. Using this relation the amount of Al incorporated into each film can be determined.

Top-view and cross-sectional morphology were imaged with a Leo 1550 Schottky source scanning electron microscope (SEM). Images were taken at an accelerating voltage of 10 or 15 kV, film thicknesses were measured with cross-sectional images.

### 3. Results and discussion

#### 3.1. Precursor films

The average composition of the precursor films determined by EPMA is given in Table 1. The films are divided into three sets, with increasing Al content as one moves from Sets 1 to 3. Average film composition of each precursor set was slightly Cu-poor to ensure p-type conductivity and avoid the formation of  $Cu_xSe$  phases at the surface of the selenized film [17]. The XRD spectra in Fig. 2 show Cu, and CuIn phases similar to those found in CuIn or CuInGa precursor films deposited by sputtering [11].  $Cu_xAl_y$  phases and Al are also found in Sets 2 and 3 precursors, and only a small  $Al_2Cu$  peak is found in Set 1 films. No oxide peaks are found in the precursor XRD scans.

A top-view SEM image of a representative precursor film shows a dark background with small grains as well as bright island agglomerations (Fig. 3). Using EDS and EPMA the darker background material has been found to be Cu-rich, while the islands protruding through the Cu-rich film are In-rich. This island formation has been noted in previous CuIn precursor work, where they find the separation between In-rich phase and Cu-rich phase is due to high interfacial energy [18,19].

The AES of a Set 3 (high Al) film is shown in Fig. 4. A surface oxide is observed, however due to the Cu capping layer it consists of Cu- and In-oxides rather than an  $Al_2O_3$ .  $Al_2O_3$  is a very stable oxide and would contaminate the final film and affect selenization reactions. Both Sets 1 and 2 films showed no  $Al_2O_3$  as well.

Indium, which is preferentially sputtered earlier in the deposition process, has diffused to the surface to a degree in this film in the form of In-rich islands seen in Fig. 3. Due to the Cu capping layer, and preferential sputtering of Al towards the top of the film, it is likely that Cu–Al phases form at the top of the film as well. These phases can be seen in the XRD spectra in Fig. 2. With much of the Cu already bound to Al the driving force for indium to move towards the surface to form Cu–In phases is minimized.

Table 1

Average compositions of precursor film sets measured with EPMA, and the standard deviation within each set.

Sample set	Cu (at%)	In (at%)	Al (at%)
1	48 ± 3	49 ± 3	3 ± 1
2	49 ± 3	38 ± 3	12 ± 2
3	49 ± 3	33 ± 4	18 ± 2

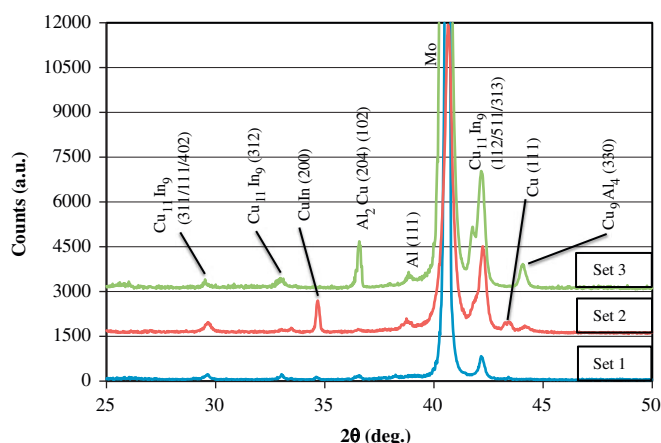


Fig. 2. XRD of CuInAl precursor films.

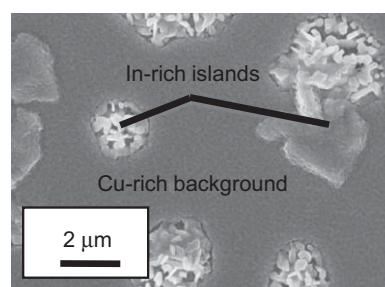


Fig. 3. Top-view SEM image of a Set 3 CuInAl precursor film.

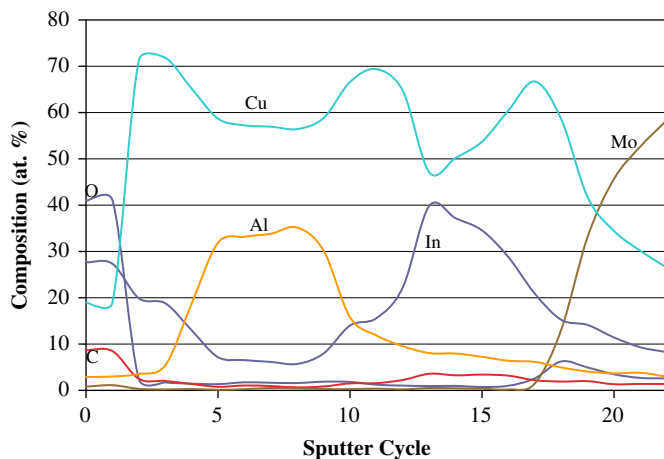


Fig. 4. AES compositional depth profile of a Set 3 precursor film.

This may be the reason why we see the majority of the indium closer to its deposited position towards the back contact. Increased In diffusion towards the surface was found as Al composition decreased. It is important to note that these films are deposited at room temperature. Increasing the substrate temperature during deposition results in greater In diffusion to the surface and greater chance of Al-oxidation.

#### 3.2. Selenized films

##### 3.2.1. Film composition and adhesion

A summary of selenization conditions, film thicknesses, and film compositions determined with EPMA are shown in Table 2.

**Table 2**

Selenization parameters for each sample along with composition determined with EPMA. The point where adhesion loss was observed is also noted.

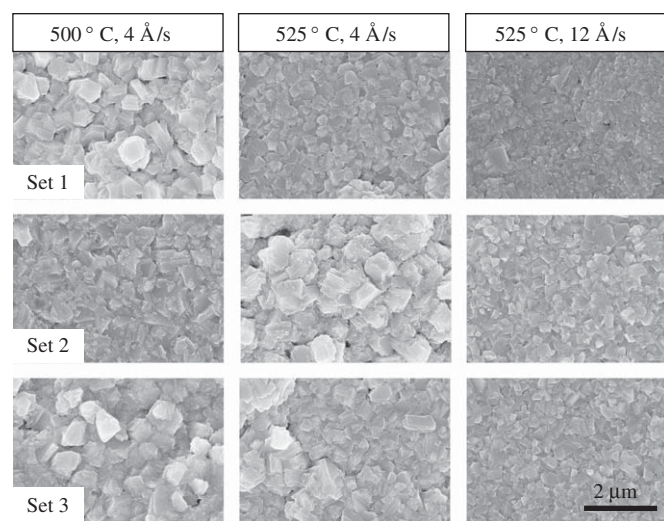
Set #	Selenization parameters				Composition				Adhesion loss
	T (°C)	t (min)	Se rate (Å/s)	Cu (at%)	In (at%)	Al (at%)	Se (at%)	(Cu+In)/Se	
<b>Thick (2–2.5 μm)</b>									
1	500	40	4	28	26	1	45	1.2	
1	500	60	4	23	28	1	48	1.06	
1	525	60	4	23	26	2	50	0.98	
1	525	60	12	21	29	0	50	1	
2	500	40	4	26	28	1	45	1.2	
2	500	60	4	24	29	1	47	1.13	
2	525	60	4	23	27	0	50	1	CdS Bath
2	525	60	12	X	X	X	X	X	Cleave
3	500	40	4	25	29	1	46	1.17	CdS Bath
3	500	60	4	26	25	2	47	1.09	CdS Bath
3	525	60	4	25	26	1	49	1.04	Selenization
3	525	60	12	X	X	X	X	X	Selenization
<b>Thin (1.5–1.75 μm)</b>									
1	500	60	4	22	28	1	48	1.04	
1	525	60	4	23	27	0	50	1	
1	525	60	12	22	28	0	49	1.02	
2	500	60	4	24	27	1	48	1.06	
2	525	60	4	23	26	1	50	0.98	
2	525	60	12	21	30	0	49	1.04	CdS Bath
3	500	60	4	22	28	1	49	1.02	CdS Bath
3	525	60	4	22	29	0	49	1.04	
3	525	60	12	22	27	0	50	0.98	Cleave

Also noted is the step during device fabrication, if any, where partial or complete adhesion loss at the CIAS/Mo interface was observed. Adhesion loss occurred either during the selenization process itself, during the cleaving of samples for characterization and finishing, or during the CdS chemical bath deposition process. There are a few trends that can be taken from this data. First, the samples with the least Al show the greatest adhesion. As Al content is increased in the films progressively worse adhesion is found. Second, thinner samples adhere better than thicker samples. And third, the 12 Å/s Se flux resulted in worse adhesion than the 4 Å/s Se flux. Two of the 12 Å/s samples lost adhesion completely during selenization or during cleaving and could not be analyzed further.

Samples selenized for 40 min were found to be selenium deficient. The reaction time was increased to 60 min to allow more time for selenium incorporation. These samples show an increase in selenium; however 500 °C samples still appear to be slightly selenium deficient. Samples selenized at 525 °C were found to have ~50% Se. There was no measurable change in at% Se between samples selenized under 4 Å/s vs. 12 Å/s Se flux, or between various thicknesses.

EPMA composition measurements show little to no Al. This suggests all the Al is at a depth greater than ~500 nm in all films, and therefore too deep for the low energy Al K $\alpha$  X-rays to escape out of the bulk. AES results will confirm that Al remains in the film at depth, however without the accuracy of EPMA it is difficult to say if the Cu/Al ratio remains the same between the precursor and selenized films.

The adhesion issues with the higher Se flux samples are likely due to the speed in which the CIS phase grew in the film. The 4 Å/s Se flux may have slowed the growth of CIS, allowing more diffusion to occur, and resulting in a more intermixed and less stressed film. The 12 Å/s Se flux would have promoted the formation of the binary selenides Cu<sub>2-x</sub>Se and InSe/In<sub>2</sub>Se<sub>3</sub>, increasing the availability of the reaction partners to form CIS [20]. This likely led to a phase separation early in the selenization process, rapid CIS growth, and a large stress between the phases that could not be supported.

**Fig. 5.** Top-view SEM images of thin selenized samples.

### 3.2.2. Film morphology and grain growth

Fig. 5 shows top-view SEM images of the thinner films. There is no significant difference between samples selenized at 500 and 525 °C at 4 Å/s. Grain size differences are probably due to small differences in Cu and Se concentration. Samples selenized with 12 Å/s Se flux appear to grow denser and smoother than the low Se flux samples.

Cross sectional images of these samples are seen in Fig. 6. All samples exhibit vertical grain growth. Moving from Sets 1 to 3 films there appears to be a secondary layer of increasing thickness that develops beneath the vertically oriented grains towards the top of the films. Voids are found both above this layer, at the interface with the large vertical grains, as well below, at the interface with the Mo grains. These voids likely resulted in the adhesion loss found with increasing Al content films.

There is no significant visible difference in void size or density at the interfaces between the 4 and 12 Å/s samples. There does appear to be smaller grains towards the back contact in the Set 1 films selenized under 12 Å/s flux which are not seen in the 4 Å/s

samples, but this is not seen in the Set 3 films. The Set 2 sample selenized under 12 Å/s completely lost adhesion before a cross section could be imaged.

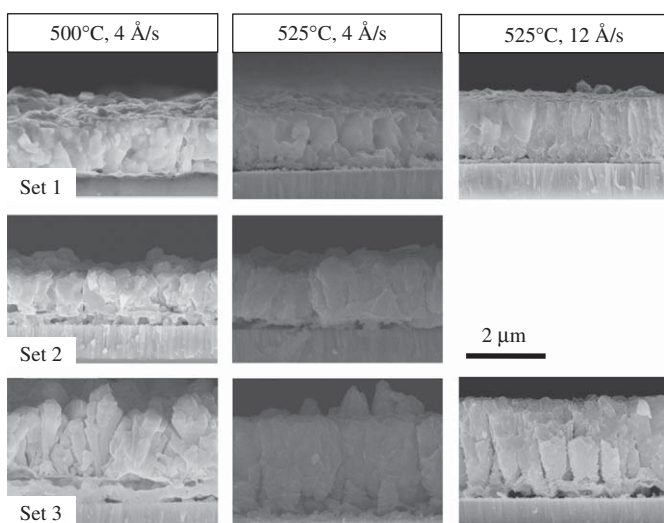


Fig. 6. Cross-sectional images of the selenized samples found in Fig. 5. The Set 2 sample selenized at 525 °C for 60 min, under 12 Å/s Se flux lost adhesion before imaging.

### 3.2.3. Compositional depth profiles

Depth profiling of selenized films revealed a number of potential film growth issues (Fig. 7). The Set 1 films selenized at 525 °C show an In-rich surface region, while Cu increases towards the back contact and Se appears to grade down with this increasing Cu. The Al in all films is either completely or partially isolated at the back contact, and present with oxygen. Set 3 films also show an increase in Cu in the region where Al and oxygen increase. These results suggest that the secondary layer found in cross-sectional SEM images in Fig. 6 consists of Al, O, and in some cases Cu.

Mild In grading is seen in the Set 1 films, but the total concentration of Group IIIb elements in the film is roughly constant, as expected. The Cu–Se grading is more pronounced. Films show the desired Cu:Se ratio at the surface, but decreasing Se in the film as depth increases. During the growth of these films In–Se and Cu–Se binary compounds form around the melting point of Se, and then combine to form  $\text{CuInSe}_2$  [21,22]. The Cu–Se in this reaction is thought to behave as a quasi-liquid fluxing agent that helps in the formation of large, dense grains. The melting point of this binary compound is 523 °C [17]. Samples selenized at 525 °C would have had this mechanism active and it

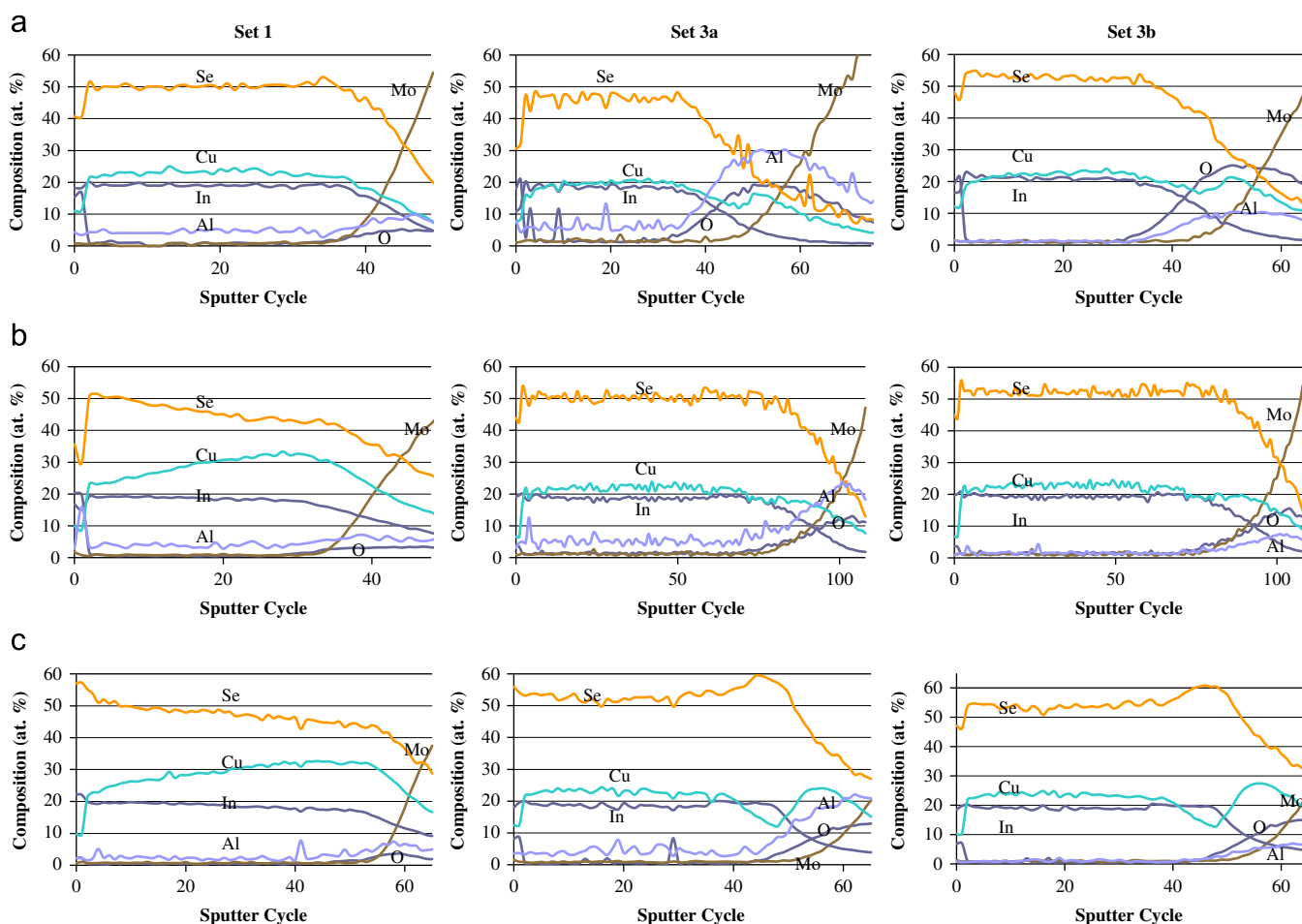


Fig. 7. AES compositional depth profiles of thin selenized films. Selenization parameters indicated by rows: (a) 500 °C, 60 min, 4 Å/s Se flux; (b) 525 °C, 60 min, 4 Å/s Se flux; (c) 525 °C, 60 min, and 12 Å/s Se flux. The column labeled Set 3a is Set 3 films calculated using the sensitivity factor for Al (0.07), and Set 3b is Set 3 films calculated with the sensitivity factor of Al in  $\text{Al}_2\text{O}_3$  (0.265).

may have altered the growth by promoting the formation of CIS at the surface more quickly. The resulting surface layer of CIS may have inhibited the further diffusion of Cu to the surface and incorporation of Se evenly throughout the film. This explanation only holds for the Set 1 films however, as this does not appear to happen in Set 3 films. There is no appreciable difference in composition between the two sets of films in the region measured by EPMA. It is possible either the large portion of Al in the Set 3 film, or small differences in Cu:In ratio combined with the increased surface CIS growth produced the increased Se-deficiency with depth.

The segregation of Al towards the back contact is not a completely unexpected phenomenon. In CIGS films formed by selenization of precursors Ga grading is seen as well [23]. In CIGS films, CIS will begin crystallizing at  $\sim 230^\circ\text{C}$ , while CGS does not form until  $\sim 300^\circ\text{C}$ . These films will then form CIGS by interdiffusion at higher temperatures [21,24]. For CIAS films high-temperature XRD measurements have found that  $\text{Al}_2\text{Se}_3$  forms around  $475^\circ\text{C}$ ,  $(\text{In,Al})_2\text{Se}_3$  around  $425^\circ\text{C}$ , and the formation of CIAS will not occur until  $480\text{--}490^\circ\text{C}$ . The reaction is assumed to proceed either directly as  $(1/2)\text{CuSe}_2 + (1/2)(\text{In,Al})_2\text{Se}_3 \rightarrow \text{CuInAlSe}_2$ , or through interdiffusion of  $\text{CuInSe}_2$  and  $\text{CuInAlSe}_2$  [22]. All these reactions occur at significantly higher temperature than the CIS reaction. The CIS and CIAS should be able to form a single-phase material by inter-diffusion, but in the temperature and time parameters investigated this does not appear to occur. XRD indicates Al/Cu–Al/ and Cu–In–Al phases remain even after 60 min of selenization at  $525^\circ\text{C}$  (Fig. 8).

The oxygen present with the Al at the back contact is also an issue in these films. Originally AES scans were performed using the preset elemental sensitivity factor for the crystalline Al KLL transition (sensitivity factor=0.07), as the expectation was that all Al was incorporated into a CIAS film (Fig. 7 columns – Sets 1 and 3a). However due to the presence of oxygen the data were recalculated using the sensitivity factor for the Al KLL transition in  $\text{Al}_2\text{O}_3$  (sensitivity factor=0.265) (Fig. 7 column – Set 3b). The Auger yield for Al in  $\text{Al}_2\text{O}_3$  is different than that of crystalline Al, and there is a slight shift down in expected peak energy from 1390 to 1385 eV. After recalculating the data using the  $\text{Al}_2\text{O}_3$  sensitivity, the Al:O ratio shifts dramatically between Sets 3a and 3b, from  $\sim 3:2$  to greater than  $2:3$ . This shift was consistent across all samples that showed oxygen. The actual Auger profile is probably a combination of the two sensitivities; with at least part of the segregated back contact Al in the form of  $\text{Al}_2\text{O}_3$ . The bulk XRD data clearly indicate the presence of both crystal structures

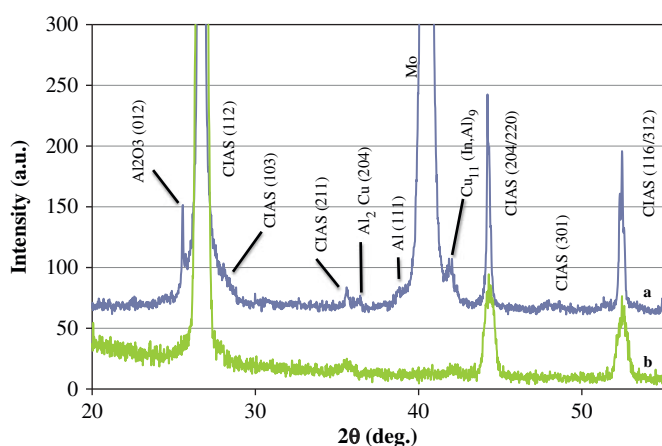


Fig. 8. XRD scans of a Set 1 film selenized at  $525^\circ\text{C}$  for 60 min with  $4 \text{ \AA/s}$  Se flux. Both  $2-\theta$  scan (a), and surface sensitive grazing-incidence scans were run (b).

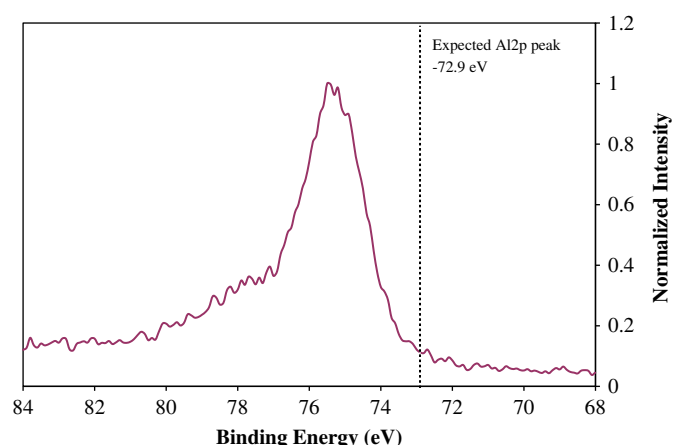


Fig. 9. XPS scan of the  $\text{Al}2p$  peak of a Set 3 sample at the CIAS/Mo interface. There is a shift in the binding energy indicating the presence of oxygen in the aluminum, likely in the form of  $\text{Al}_2\text{O}_3$ .

in the films as well, while these peaks disappear in GIXRD scans. Any Al present towards the surface must be incorporated into the CIAS lattice.

To analyze the oxygen-rich back surface XPS was run on the Set 3 sample seen in the top row of Fig. 7. The innermost area of the sputter crater was analyzed, right above the exposed Mo. The only shift found in the scans occurred for aluminum. The expected binding energy for  $\text{Al}2p$  is  $72.9 \text{ eV}$ , with the observed peak at  $\sim 75.3 \text{ eV}$ . The results indicate the presence of what is either  $\text{Al}_2\text{O}_3$ , or a combination of aluminum oxide and aluminum [25] (Fig. 9). The lack of a clear Al peak suggests the oxidized Al and crystalline Al found in XRD results are not present together, and instead are scattered in pockets towards the back surface of the film. No other oxides were found.

The source of the oxygen for  $\text{Al}_2\text{O}_3$  formation is not immediately clear. Since oxygen was only found as Cu and In surface oxides in the precursor films we assume this is not the source of the contamination. The most obvious source is the oxygen present in the form of water vapor in the vacuum system. Since the system is not load-locked each sample change introduces water vapor, which is not easily removed by the turbo pump, and cannot be baked-out without heating the precursor films. If Al or  $\text{Al}_2\text{Se}_3$  were exposed to water vapor  $\text{Al}_2\text{O}_3$  could be formed. The  $\text{Al}_2\text{Se}_3 + 3\text{H}_2\text{O} \rightarrow \text{Al}_2\text{O}_3 + 3\text{H}_2\text{Se}$  reaction, or the  $2\text{Al} + 3\text{H}_2\text{O} \rightarrow \text{Al}_2\text{O}_3 + 3\text{H}_2$ ;  $\text{H}_2 + \text{Se} \rightarrow \text{H}_2\text{Se}$  reaction would also produce toxic hydrogen selenide gas. The Cu and In selenides, as well as CIS that forms initially should act as a diffusion barrier preventing the Al from reacting with oxygen sources in the vacuum, however if any Al was exposed during deposition this could be the source of contamination. The  $\text{Al}_2\text{Se}_3$  reaction could also explain the difficulty in incorporating adequate Se in the films, as the selenium may be removed in the form of  $\text{H}_2\text{Se}$  by the pumping system.

Oxygen could also have diffused through the Mo from the soda-lime glass substrate [26]. It seems unlikely that the volume of oxygen found in the Set 3 films would have diffused through the Mo grains, but this may have been a contributing source.

Oxygen present in the auger system could have contaminated any elemental Al in the film once exposed by ion sputtering. An experiment was performed using a DC-sputtered Al film, scanning and sputtering under the same time period as was used in Auger depth profiles. Though a small degree of oxygen was found to react in the time between sputtering and analysis this was never more than a few percent. Not enough to account for the oxygen seen in Sets 2 and 3 films.

### 3.2.4. (1 1 2) peak analysis

An analysis of the (1 1 2) peaks showed an interesting trend in the data (Fig. 10). Based on the amount of Al in the precursor films the (1 1 2) peaks for Set 1 are expected at  $\sim 26.77^\circ$ , Set 2  $\sim 26.89^\circ$ , and Set 3  $\sim 27.08^\circ$ , calculated from Vegard's law. This would be the case for a single-phase material with all Al present in the precursor incorporated into the sample. Other than the Set 1 sample selenized at  $500^\circ\text{C}$  this does not occur under these experimental conditions.

It appears all the samples selenized at  $500^\circ\text{C}$  incorporate more Al into the CIS structure than their higher temperature counterparts. However, the expected trend would be for more Al to incorporate at  $525^\circ\text{C}$  rather than  $500^\circ\text{C}$  due to greater inter-diffusion at higher temperatures. The peak seen in these  $500^\circ\text{C}$  samples is likely either a Se-deficient phase, or an indium-rich/Cu-poor phase. Either would agree with the composition results obtained with EPMA, and expected shifts according to PDF files (79-2208, 79-2207). In the indium-rich case this would be due to the excess of indium readily available to react with Se and Cu, and the relative difficulty in incorporating the available Al at this temperature or breaking the Cu–Al bonds that have formed.

At  $525^\circ\text{C}$ , there is a shift in the peaks towards the expected CIS peak at  $26.624^\circ$ . These samples appear to show a distinct phase separation, especially in the Sets 1 and 3 samples. These phases are either a low- and high-Al CIAS phase, or a low-Al CIAS phase with a phase similar to that seen in the  $500^\circ\text{C}$  case. The results from the thick samples are not shown, but similar trends were found.

This data, along with AES measurements and SEM cross-sections, explain many of the adhesion issues found. Adhesion is progressively worse moving from Set 1 (low-Al) to Set 3 (high-Al).

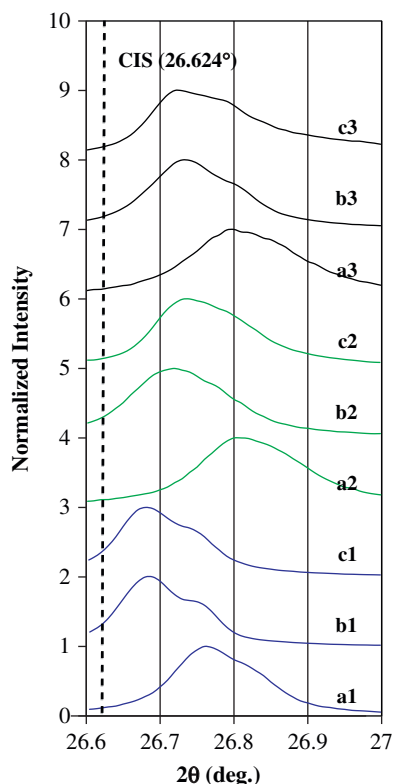


**Fig. 10.** XRD scans of the (1 1 2) peak showing the shift in peak location for all thinner samples. Numbers 1, 2, and 3 refer to Set 1, Set 2, and Set 3, respectively. Selenization conditions are labeled as (a)  $500^\circ\text{C}$ , 60 min,  $4 \text{ \AA/s}$  Se flux, (b)  $525^\circ\text{C}$ , 60 min,  $4 \text{ \AA/s}$  Se flux, and (c)  $525^\circ\text{C}$ , 60 min,  $12 \text{ \AA/s}$  Se flux. The expected peak location for CIS is included as a reference.

The Al has not fully incorporated into any of the produced films; instead much of it has formed a secondary layer between the Mo and CIAS that is at least partly oxidized. As Al-content is increased the thickness of this layer also increases, resulting in an increase in voids at this interface. Thicker samples contain more Al relative to thinner samples. As a result the interface layer grows thicker, which likely resulted their relatively worse adhesion. Without alleviating the oxygen problem and incorporating the Al into the bulk film a quality back-contact/absorber interface cannot be produced.

### 3.2.5. Device testing

Complete devices were formed on samples without adhesion loss and tested under AM1.5 conditions. The best device efficiency was found to be 5.2% for a thin Set 1 film selenized at  $500^\circ\text{C}$  for 60 min. Open circuit voltage for this device was 0.465 V, short circuit current was  $33.03 \text{ mA/cm}^2$ , and the fill factor was 33.91%. All other devices failed to produce power. We attribute these failures to the highly resistive Al–Al<sub>2</sub>O<sub>3</sub> layer and the resulting voids that appear to have formed at the interface between the absorber and Mo.

## 4. Conclusions

Mixed phase CIAS films have been deposited by co-sputtering of CuInAl precursors followed by selenization with elemental selenium vapor. While precursor films can be deposited free of bulk oxygen, oxidation cannot be avoided under the conditions used during selenization. Higher Se flux ( $12 \text{ \AA/s}$ ) was found to favor CIS growth and result in poor adhesion compared with  $4 \text{ \AA/s}$  flux. Limited aluminum incorporation occurred at both selenization temperatures ( $500$  and  $525^\circ\text{C}$ ) and both heating times (40 and 60 min). A longer duration and/or higher temperature selenization process should result in more diffusion of Al into the CIAS film; however increasing either of these parameters is not ideal for production environments. Longer selenization times could result in a bottleneck in the production process. Higher temperatures increase energy needs and prevent the use of CIAS as a tandem top cell unless a superstrate setup is engineered.

Another option would be to further thin the films, which would result in a faster selenization process since diffusion lengths are decreased and less material needs to be reacted. This may be a better option for a tandem configuration, as the top absorber will not need to be as thick as a typical single cell absorber ( $\geq 1 \mu\text{m}$ ). High temperatures ( $\geq 500^\circ\text{C}$ ) will still be needed however to form the CIAS film.

## Acknowledgements

The authors would like to thank Richard Moore of the College of Nanoscale Science and Engineering (CNSE) for his assistance with XPS measurements and discussions on AES data, as well as Dr. Eric Lifshin of CNSE for discussions on EPMA data. We would also like to thank Stephen Glynn and Clay DeHart of the National Renewable Energy Laboratory (NREL) for their help with device finishing and useful comments on the finishing process, as well as Dr. Rommel Noufi of NREL for useful discussions. This work was supported by the New York State Foundation for Science, Technology and Innovation (NYSTAR).

## References

- [1] D. Marron, A. Marti, A. Luque, Thin-film intermediate band chalcopyrite solar cells, *Thin Solid Films* 517 (2009) 2452–2454.

- [2] U. Rau, M. Schmidt, A. Jasenek, G. Hanna, H.W. Schock, Electrical characterization of Cu(In,Ga)Se<sub>2</sub> thin-film solar cells and the role of defects for the device performance, *Solar Energy Materials and Solar Cells* 67 (2001) 137–143.
- [3] M. Gloeckler, J.R. Sites, Efficiency limitations for wide-band-gap chalcopyrite solar cells, *Thin Solid Films* 480–481 (2005) 241–245.
- [4] T. Minemoto, T. Matsui, H. Takajura, Y. Hamakawa, T. Negami, Y. Hashimoto, T. Uenoyama, M. Kitagawa, Theoretical analysis of the effect of conduction band offset of window/CIS layers on performance of CIS solar cells using device simulation, *Solar Energy Materials and Solar Cells* 67 (2001) 83–88.
- [5] G. Hanna, A. Jasenek, U. Rau, H.W. Schock, Influence of the Ga-content on the bulk defect densities of Cu(In,Ga)Se<sub>2</sub>, *Thin Solid Films* 387 (2001) 71–73.
- [6] J.T. Heath, J.D. Cohen, W.N. Shafarman, D.X. Liao, A.A. Rockett, Effect of Ga content on defect states in CuIn<sub>1-x</sub>Ga<sub>x</sub>Se<sub>2</sub> photovoltaic devices, *Appl. Phys. Lett.* 80 (2002) 4540–4542.
- [7] J. Heath, J. Cohen, W. Shafarman, Defects in copper indium aluminum diselenide films and their impact on photovoltaic device performance, *Mater. Res. Soc. Symp. Proc.* 763 (2003) B92.1–B92.6.
- [8] P.D. Paulson, M.W. Haimbodi, S. Marsillac, R.W. Birkmire, W.N. Shafarman, CuIn<sub>1-x</sub>Al<sub>x</sub>Se<sub>2</sub> thin films and solar cells, *J. Appl. Phys.* 91 (2002) 10153–10156.
- [9] S. Marsillac, P.D. Paulson, M.W. Haimbodi, R.W. Birkmire, W.N. Shafarman, High-efficiency solar cells based on Cu(InAl)Se<sub>2</sub> thin films, *Appl. Phys. Lett.* 81 (2002) 1350–1352.
- [10] F. Dhlamini, Optimization of the structural properties of selenized metallic alloys, *Magister Scientiae Dissertation* (2003).
- [11] B. Mhlungu, Deposition of single-phase Cu(In,Ga)Se<sub>2</sub> thin films, *Magister Scientiae Dissertation* (2004).
- [12] F.O. Adurodiya, S.K. Kim, S.D. Kim, J.S. Song, K.H. Yoon, B.T. Ahn, Characterization of co-sputtered Cu–In alloy precursors for CuInSe<sub>2</sub> thin films fabrication by close-space selenization, *Solar Energy Materials and Solar Cells* 55 (1998) 225–236.
- [13] T. Nakada, Akio Kunioka, Sequential sputtering/selenization technique for growth of CuInSe<sub>2</sub> thin films, *Jpn. J. Appl. Phys.* 37 (1998) L1065–L1067.
- [14] D. Dwyer, I. Repins, H. Efstathiadis, P. Haldar, Deposition of CuInAlSe<sub>2</sub> films using co-sputtered precursors and selenization, in: *Proceedings of the 34th Photovoltaic Conference*, 2009, pp. 000247–000251.
- [15] J. Goldstein, D. Newbury, D. Joy, C. Lyman, P. Echlin, E. Lifshin, L. Sawyer, J. Michael, in: *Scanning Electron Microscopy and X-ray Microanalysis*, Springer Science and Business Media Inc., 2003.
- [16] L. Vegard, Die Konstitution der Mischkristalle und die Raumfüllung der Atome, *Z. Phys.* 5 (1921) 17–26.
- [17] N. Dhere, Present status and future prospects of CIGSS thin film solar cells, *Solar Energy Materials and Solar Cells* 90 (2006) 2181–2190.
- [18] C.H. Chung, S.D. Kim, H.J. Kim, F.O. Adurodiya, K.H. Yoon, J. Song, Phase formation and control of morphology in sputtered Cu–In alloy layers, *Solid State Communications* 126 (2003) 185–190.
- [19] O. Volobujeva, M. Altosaar, J. Raudoja, E. Mellikov, M. Grossberg, L. Kaupmees, P. Barvinschi, SEM analysis and selenization of Cu–In alloy films produced by co-sputtering of metals, *Solar Energy Materials and Solar Cells* 93 (2009) 11–14.
- [20] J. Djordjevic, E. Rudigier, R. Scheer, Real-time studies of phase transformations in Cu–In–Se–S thin films – 3: selenization of Cu–In precursors, *J. Cryst. Growth* 294 (2006) 218–230.
- [21] W.K. Kim, E.A. Payzant, S. Yoon, T.J. Anderson, In situ investigation on selenization kinetics of Cu–In precursor using time-resolved, high temperature X-ray diffraction, *J. Cryst. Growth* 294 (2006) 231–235.
- [22] S. Jost, F. Hergert, R. Hock, M. Purwins, R. Enderle, Real-time investigations of selenization reactions in the system Cu–In–Al–Se, *Phys. Status Solidi A* 203 (2006) 2581–2587.
- [23] B. Basol, V. Kapur, A. Halani, C. Leidholm., J. Sharp, J. Sites, A. Swartzlander, R. Matson, H. Ullal, Cu(In,Ga)Se<sub>2</sub> thin films and solar cells prepared by selenization of metallic precursors, *J. Vac. Sci. Technol. A* 14 (1996) 2251–2256.
- [24] W.K. Kim, E.A. Payzant, T.J. Anderson, O.D. Crisalle, In situ investigation of the selenization kinetics of Cu–Ga precursors using time-resolved high-temperature X-ray diffraction, *Thin Solid Films* 515 (2007) 5837–5842.
- [25] T.J. Chuang, K. Domen, Ultraviolet laser excited adsorbate–surface interactions: NH<sub>3</sub>, C<sub>2</sub>H<sub>4</sub>, and CH<sub>2</sub>I<sub>2</sub> on Al and oxidized Al surfaces, *J. Vac. Sci. Technol. B* 7 (1989) 1200.
- [26] D. Fisher, I. Repins, J. Schaefer, M. Beck, W. Batchelor, M. Young, S. Asher, The effect of Mo morphology on the performance of Cu(In,Ga)Se<sub>2</sub> Thin Films, NREL Document.